Canadian Science Publishing
NRC Research Press journals | Publishing Services

Canadian Geotechnical Journal
Revue canadienne de géotechnique

Managing Rockfall Risk through Baseline Monitoring of Precursors with a Terrestrial Laser Scanner

Journal:	*Canadian Geotechnical Journal*
Manuscript ID	cgj-2016-0178.R1
Manuscript Type:	Article
Date Submitted by the Author:	04-Sep-2016
Complete List of Authors:	Kromer, Ryan; Queen\'s University, Geological Sciences and Geological Engineering Lato, Matthew; BGC Engineering Hutchinson, D. Jean; Queen's University, Geological Science and Geological Engineering Gauthier, David; BGC Engineering Edwards, Thomas; CN Railway, Design & Construction
Keyword:	Terrestrial Laser Scanning, Rock Slope Hazard, Landslide Risk, Rockfall, Risk Assessment

Managing Rockfall Risk through Baseline Monitoring of Precursors with a Terrestrial Laser Scanner

Ryan Kromer[1], Matt Lato[2], D. Jean Hutchinson[1], Dave Gauthier[2], Tom Edwards[3]*

1. Department of Geological Sciences and Geological Engineering, Miller Hall, Queen's University, Kingston, Canada, K7L 3N6

2. BGC Engineering, 414 Princeton Ave., Ottawa, Canada, K2A 4G2

3. Canadian National Railway, 10229–127 Avenue, Edmonton, AB T5E 0B9, Canada

** Corresponding Author: ryan.kromer@queensu.ca, 1-613-533-3388*

Abstract

Rockfalls represent significant risks to safe and efficient use of transportation corridors. In this paper we address the management of rockfall risk through baseline remote monitoring of susceptible slopes (every 2-4 months) along a transportation corridor along the Fraser River Valley in western Canada with a terrestrial laser scanner and supporting remote sensing technologies. This includes identifying potential rockfall source zones based on incipient signs of failure, tracking kinematics in 3D to better understand the mechanism of failure, estimating potential failure volumes based on bounding joint structure and transmitting this information to the railway operator for an assessment of risk. We demonstrate our approach for one case along the line where we identified several potential failures ranging in volume from 48 m^3 to 4200 m^3. Our projections of the location of failures were successful, in that volume projections were within 10-55%, and the anticipated kinematics and failure mechanism were consistent with the assessment of post failure rockfall scar geometries. Accurate volume and kinematics estimates are important for the assessment of hazard, risk and the planning of risk mitigation options. In general, this approach can be used to better manage risk from rockfall hazard in communities, transportation corridors or other infrastructure.

Les dangers d'éboulement rocheux représentent l'un des risques les plus importants affectant les infrastructures situées dans les terrains montagneux. Nous recherchons la gestion des risques des dangers d'éboulement rocheux avec la surveillance de base (chaque 2-4 mois) avec un scanner laser terrestre et autre technologie supportant le long d'un corridor ferroviaire situer dans L'Ouest canadien. Le but de cette étude est d'identifier les zones de déformation avant la rupture de la roche, de suivre les zones de déformation en 3D pour mieux comprendre le mécanisme de rupture, de calculer les volumes potentiels, ainsi que de transmettre l'information a la compagnie

de chemin de fer pour une évaluation de risque. On montre que notre approche pour quatre blocs avec volumes entre 48 - 4200m^3 qui étaient analysés avant les ruptures se soit produite. Analyse de la pente après les ruptures nous avons indiqué qu'il y avait un bon accord avec les projections de mécanisme et une erreur entre 10-55 % pour les volumes. L'identification de la location, la mécanique et volume potentiel en avance des chutes de blocs a résulté en une meilleure gestion de la priorisation des efforts de réduction des impacts, en une réduction des risques, ainsi qu'en une amélioration de la compréhension des mécanismes précurseurs à la rupture en général.

Key Words: Risk Assessment, terrestrial laser scanning, rock slope hazard, landslide risk management

Introduction

Transportation corridors, infrastructure, and communities are exposed to various geological hazards, including rock slope failures. These failures result from natural and man-made processes and their occurrence can be sudden and unexpected. Potential rock slope failures are present in a wide variety of different terrains, making them difficult hazards to manage and it is a challenge to anticipate the location and time of failure in advance. As a result, rock slope failures pose significant risks to transportation corridor infrastructure and the travelling public (Hungr et al. 1999; Peckover and Kerr 1977).

As part of a collaborative effort between the Canadian government, industry and universities, under the umbrella of the Railway Ground Hazard Research Program, we have been monitoring a selection of hazardous slopes across the Canadian rail network using Terrestrial Laser Scanning (TLS), Terrestrial Photogrammetry, Oblique Aerial Photogrammetry (OAP), and Aerial Laser Scanning (ALS) (Lato et al. 2011; 2014; Kromer et al. 2015a).These approaches can aid in risk assessment by:

1. Providing a higher degree of safety to personnel managing risk from rock slope hazards as data can be collected remotely.
2. Allowing the efficient collection of vast amounts of high resolution data of previously inaccessible areas (Oppikofer et al. 2008; Stock et al. 2011; Sturzenegger and Stead 2009).
3. Providing frequent data collection and the observation of change, including frequencies, locations and characteristics of rock movement events (Jaboyedoff et al. 2012; Abellán et al. 2014).

TLS is particularly advantageous technology for slope monitoring and hazard assessment. It can be used to monitor a large number of sites along transportation corridors or other elements at risk at a baseline level (monthly, bimonthly, for example). In some circumstances, it is possible to detect millimetre-level changes by taking advantage of point redundancy (Abellán et al. 2011; Kromer et al. 2015b; Lague et al. 2013), and extract 3D deformation vectors through tracking the 3D movement of an object (Oppikoffer et al. 2009; Teza et al. 2007). It is a relatively affordable and versatile technique as compared to other slope scale rockfall monitoring approaches (Lato et al. 2015). Comparison of point clouds collected from TLS can also be used to identify signs of progressive failure of a rock slope allowing the identification of potential failure locations (Abellán et al. 2010). These precursor signs include deformation, sometimes ending in an observed acceleration period (Royán et al. 2015), the development of tension cracks or other fractures (Kromer et al. 2015a; Stock et al. 2012) and precursor rockfalls concentrated along the perimeter of the progressively developing failure (Kromer et al. 2015a; Rosser et al. 2007; Royán et al. 2015; Stock et al. 2012) that ultimately define the evolution of the slope (Royán et al. 2013).

We propose the inclusion of quantitative rockfall precursor observations in the risk management process using baseline monitoring with TLS. The focus of this monitoring is on detecting incipient signs of failure known as the detachment or the damage accumulation phase of failure (Sättele et al. 2015). By detecting these precursor signs, we can assess the hazard, defined as the spatial and temporal probability of rockfall failure of a particular size or intensity (Hungr et al. 1999; Corominas et al. 2013), by locating areas showing precursor signs of failure, and estimating the potential volume, kinematics and relative likelihood of failure. Temporal probability is generally analyzed based on historical magnitudes and frequencies and represents

an average for an area and not a probability for a specific location (Frayssines and Hantz 2006; Hungr et al. 1999). In our framework, we assume that areas showing precursors signs have a much higher spatial and temporal likelihood of failure than the slope average, essentially providing a long term or very early warning of failure.

The aim of this study is to use TLS monitoring at a baseline level (bi-monthly) and other supporting remote sensing technologies, to demonstrate how the proposed framework can improve risk management along transportation corridors exposed to rock slope hazards, by providing assessments and warning of incipient rock slope failure and engineering parameters necessary to guide risk mitigation efforts. We demonstrate our approach for one rock slope prone to failure located along the CN mainline track in western Canada, which has been monitored for an 809-day period at the time of writing.

Study Site Description

The case history site discussed in this paper consists of a geomorphologically complex rock slope, with a mean angle ranging from 45 to 55°, that is located along the CN rail line 150 km northeast of Vancouver within the Fraser River valley, at railway mile 109.4 of the Ashcroft subdivision. In November 2012, a 53 000 m^3 rockslide occurred, resulting in the destruction of a 21 m long rockfall protection structure, the burial of a 100 m section of track and a four-day interruption in rail service. A more detailed description of the failure can be found in Sturzenegger et al. (2014) and of the remediation work in Lato et al. (2014). Several remote sensing technologies were also combined at this site for mapping change in mountainous terrain by Lato et al. (2014).

Geologically, the slope is composed of a thick succession of Cretaceous-aged shallow water deltaic sedimentary rocks, described in detail by MacLaurin et al. (2011). Sturzenegger et al. (2014) describe two local scale faults that cross cut the slope and four main joint sets (J1-J4 dip dir. /dip: 069° /88°, 120° /85°, 252° /44° and 031° /84°), Figure 1, bottom right. The structure of this slope results in various failure styles, including sliding, wedge and toppling failures.

Figure 1

Data Collection

A combination of complementary remote sensing technologies was used throughout the study as discussed by Lato et al. (2015). Aerial laser scanning data was collected from a fixed wing aircraft in November 2012 and April 2014. We used these data for the structural characterization and to detect change over a wide area of the rail corridor. We have collected high resolution terrestrial laser scanning data on a periodic basis since 28 November 2013 from a positon on the opposite (west) side of the Fraser River valley; utilizing the TLS data for detailed change detection and to identify failure precursors (deformation, precursor rockfalls and tension cracks opening) using the techniques and logic described by Kromer et al. (2015a). We collected a total of 15 TLS scans, including multiple scans during some campaigns for redundancy and error checking, spanning nine time intervals between collection campaigns (Figure 2). We collected high resolution photography from the same location using a Gigapan robotic head for creation of high-resolution panoramic images of the slope, as in Stock et al. (2011) and Lato et al. (2012). After several rockfall events in December 2014, we collected oblique photos from a helicopter (OAP-H) to construct a model for a post failure assessment of rock runout and integrity of the rail infrastructure.

We collected TLS data using an Optech Ilris 3D-ER scanner. This scanner has a range of 1800 m at 80% surface reflectivity and a manufacturer-specified range and angular accuracy at 100 m per point of 7 mm and 8 mm, respectively (Teledyneoptech 2014).The area of the slope we monitored with TLS, shown in Figures 1 and 2, ranges from 185 to 340 m a.s.l. and spans a 200 m length of railway track. We collected TLS data from two stations located on the opposite side of the river valley, providing overlapping coverage of the area of interest, with a minimum and maximum range to slope (bottom and top) of 350 and 550 m respectively. The spacing between data points is therefore between 0.05 and 0.08 m. We collected 162 oblique aerial photographs of the post failure slope on 14 December 2014, using a Nikon D800 camera equipped with a 50 mm (f/1.8G) Nikon lens. CN Rail procured the ALS data and the supplier processed the raw data, as detailed in Lato et al. (2014).

Data Processing and Analysis

Terrestrial Laser Scanning Data Processing

We used IMAlign (InnovMetric 2014) to register each successive TLS scan to the baseline reference scan from 28 November 2013. We used a three step alignment procedure consisting of: (i) manual identification of common points, (ii) implementation of the PolyWorks' iterative surface matching algorithm which is based on the iterative closest point (ICP) best fit algorithm (Besl and McKay 1992), and (iii) identification and omission of areas of slope change followed by a reapplication of the best fit algorithm. We omitted all data points affected by the construction of the rockfall protection structure, seen in Figure 1, from the alignment process. Interscan alignment error (1 St. Dev) between TLS scans varied from 0.011 to 0.018 m.

Structure from Motion Photogrammetry Data Processing

We used oblique aerial photos collected from a helicopter (OAP-H) to build a 3D point cloud and meshed surface model using Photoscan (V1.021) (Agisoft 2014). We omitted alignment tie-points with reprojection errors greater than 0.5 pixels from the optimized camera alignments. To coarsely scale and register the meshed surface model, we used location data provided by a GPS peripheral to the camera. We used the ICP routine in Cloud Compare (Cloud Compare 2014) software with scale adjustment for fine alignment with the TLS data. The residual cloud to mesh differences between the photogrammetry model and the TLS data, ignoring areas of significant slope change, resulted in a distribution with mean 0.00 m and standard deviation of 0.06 m.

Structural Analysis

We analyzed the slope structure surrounding deforming areas and behind failure zones using IMInspect by manually selected points belonging to a joint or failure plane and using a best fit algorithm to fit a plane to the selected points. We used these results in the estimation of potential failure volume, in combination with the 3D tracking analysis to estimate pre-failure kinematics and to measure post-failure scar structure.

Change Detection, Hazard Identification and Deformation Monitoring

To detect change smaller than the limit of detection for a single point (0.022 to 0.036 m), we implemented the spatial portion of the change detection and filtering algorithm outlined in Kromer et al. (2015b). The algorithm calculates differences along a slope dependent vector as discussed by Lague et al. (2013) and filters point cloud differences using the median of neighboring difference values, as in Abellán et al. (2009). The filtered differences are mapped on to the reference point cloud with a location index. We used a 2 m radius to calculate the slope dependent comparison vectors and 80 neighboring points for filtering of the differences for this

196 slope. Differences in a direction towards the scanner positon were assigned a positive value, and
197 differences radiating away from the scanner position were assigned a negative difference value.

198 We assessed error by analyzing point cloud differences for stable areas of the slope measured on
199 different dates, for example, at the tunnel portal entrance or at unchanged sections of outcrop,
200 and by comparing differences from repeat scans from the same date where no significant change
201 is assumed to have occurred. We found that comparison means were less than 1 mm and the
202 standard deviations of the compared differences were as low as 2.5 mm at the bottom of the
203 slope and as high as 7 mm at the top portion of the slope. Based on this analysis we define a
204 conservative limit of detection as the 95% ($LoD_{95\%}$) confidence of 12 mm, which is used to
205 display slope change spatially. We also recorded the standard deviation of the means calculated
206 from the neighbourhood filtering. This allowed us to calculate a per point or location specific 95
207 % confidence interval.

208 The filtered cloud to cloud differences were interpreted to be the result of accumulations of soil
209 or rocky debris, rockfalls, tension crack opening, discrete block deformation, vegetation growth
210 or related to human/construction activity. For example, accumulation of debris at the base of the
211 slope generates a conical shape and characteristic surface roughness, generating a positive
212 difference. Block deformation usually appears as a positive deformation, on discrete rock blocks,
213 as it moves away from the slope towards the scanner positon. Rocks that detach from a portion of
214 the slope appear as negative differences and a corresponding positive difference (accumulation)
215 is usually found downslope from the source area. Tension crack opening is distinguished from
216 rockfall as it is associated with the movement of discrete rock blocks and no corresponding
217 accumulation is found below. Errors greater than the 95% confidence interval that are the result
218 of low incidence angle, poor surface reflectance or the presence of vegetation were distinguished

by their implausible kinematics, or systematic expression, for example linear change features or errors concentrated on planes at oblique angles to the scanner line of sight. We also used the high resolution photographs and observations from track maintenance employees to aid in the interpretation of measured point cloud differences.

3D Movement Tracking Analysis

We obtained the deformation vector magnitude and direction by using three dimensional block tracking (Teza et al. 2007; Oppikofer et al. 2009). We used the ICP algorithm (Besl and McKay 1992) to fit the reference point cloud representation of the deforming block to each representation of the block in successive point clouds, followed by the extraction of the deformation magnitude and directions from the affine transformation matrices. Compared to the slope dependent normal vector, this analysis gives the true deformation direction of the central point of the chosen blocks.

Errors in this method depend on several factors, including the number of points describing the moving block and its size and shape. Very small blocks, or blocks containing too few points, may result in convergence of the ICP on an incorrect location or local minimum. We assessed error by performing the alignment method on 10 stable areas of representative size and shape located across the slope for various collection dates. Mean error in the magnitude is 0.007 m in the vertical plane and 0.005 m in the horizontal plane. Errors of the deformation magnitude, topple angle and tilt angle are fixed, whereas the trend and plunge of deformation, and azimuth of topple are dependent on the deformation magnitude and the topple magnitude, respectively, as

described by Oppikoffer et al. (2009). We present the calculated errors alongside the results for each block and comparison interval.

Assessment of Rockfall Volumes

We estimated volume of potential rockfalls from the identified surface representations of the deforming areas, the surrounding defining discontinuities and the volume of overlying surficial material. This was then compared to the volume that eventually failed. We calculated the volume of failed material by comparing pre-failure models with post failure models, either TLS to TLS or TLS to OAP-H, using the 3D methodology described in Rabatel et al. (2008).

Uncertainty in calculating the rockfall volumes results from the presence of occluded areas and the quality of the surface meshes used to generate the volume estimate. Uncertainty in the surface mesh arise from the procedure used to generate the mesh, errors specific to the TLS equipment and survey related errors, e.g. distance to target, incident angle, atmospheric conditions. As a result, there is a relative volume error which depends on the ratio of rockfall surface area to volume ratio. Rockfall shapes which include higher surface area to volume ratios result in higher relative errors. For this study, we estimated error resulting from the surface by multiplying the $LoD_{95\%}$ of the surface by the surface area. We report volumes as order of magnitude estimates to account for occlusion uncertainty, e.g. 4200 m^3 +/- 50 m^3 or 210 m^3 +/- 5 m^3. In all cases however, the uncertainty in estimating volume based on appropriate bounding joint structure is much greater than the volume measurement uncertainty. We assess the relative accuracy of our volume estimates by comparing our pre-failure estimates with measured post-failure volumes.

Timeline of Events

A detailed timeline of events including data collection, warning to railway operators, and failures is presented in Figure 2. The construction of the rockfall protection structure commenced in October 2013 and was completed in June 2014. We identified three discrete areas of rock deformation after 279 days of monitoring. These three areas are labelled A, B and C in Figure 2. On 09 September 2014, we provided detailed information to CN of the largest identified expected rockfall source area (Area A), which included the location of failure, its potential volume and kinematics of motion.

CN conducted a risk assessment using the information we provided and determined that the new rockfall protection structure would provide sufficient protection to the railway. We continued to monitor the slope in the fall of 2014 and noted continued deformation of the identified Areas A, B and C prior to failure.

On 03 December 2014, during regular track inspection, a CN engineer noted an accumulation of approximately 20-30 m^3 of rock debris in a draped steel mesh fence located above the newly built protection structure. Following three days of heavy rainfall, totaling 41 mm (Environment Canada, 2014), on 11 December 2014 a CN maintenance employee noticed a large accumulation of debris behind the rockfall protection structure.

We were able to assess the rockfall source zones and rockfall run out within three days of the observed accumulation by using the detailed 3D photogrammetric slope model generated from oblique aerial photographs taken from a helicopter (OAP-H) on 14 December 2014. We found that failure had occurred at all of the sites A, B and C. Subsequently the south (railway west

direction) end of the rockfall protection structure was modified by adding a draped catchment fence to channel debris away from the side of the structure to prevent overtopping.

The TLS data collected on 17 February 2015 revealed areas of deformation adjacent to each of the failed Areas A, B and C. We informed CN of these areas on 03 March 2015. Due to the lower resolution and limit of detection of the photogrammetry model ($LoD_{95\%}$ 0.12 m) we were not able to detect deformation by comparison with the model obtained on 14 December 2014 with confidence. Subsequent data collections revealed no further increase in deformation.

Following our analysis of the data collected on 29 March 2015 we identified a new area of deformation (Area D) and notified CN engineers. Continued monitoring of this area revealed the opening of a tension crack, a pattern of rockfall surrounding the perimeter of the deforming area and continuation of the observed deformation. We identified two additional areas of possible deformation (Areas E and F) after analysis of data collected on 22 October 2015.We transmitted this information to CN on 18 November 2015. We later re-interpreted these areas using a combination of photographs and TLS change detection and found that these areas were accumulations of sediment on top of the rock outcrop due the presence of a sediment source area above, its characteristic tear drop shape and surface roughness.

Finally, between 22 October 2015 and 15 February 2016, the blocks at Area D failed, permitting an assessment of the quality of the pre-failure volume and kinematic projections.

Figure 2

Initial Projections and Failure Warning

The point cloud differences for the three deformation areas identified in September 2014 are presented in Figure 3 and are labelled as A, B and C. There was observable deformation in all three areas in the 28 November 2013 to 04 June 2014 comparison interval (Figure 3, top inset).

The deformation at A is characterized by a group of blocks bounded by four discontinuity sets (dip dir. /dip: 115°/43°, 145° /85°, 103° /74°, 225° /70°). Blocks formed by joints sets in the central portion of the area appear to deform together, while blocks that are on the outer perimeter are characterized by a lower magnitude of deformation. We interpreted point cloud differences directly upslope of Area A to be the result of movement of soil associated with the deformation of the rock blocks. This makes the interpretation of the block deformation difficult because the soil appears to overtop the group of blocks, see Figure 3, Area A deformation series. Based on the area of interpreted deformation and the bounding joint sets, we calculated a projected volume of failure of 4800 m^3 of combined rock and soil.

Point cloud differences at Area B indicate deformation from three distinct planar blocks with a slope face plane orientation of dip dir. /dip: 223^o /73^o. Area C consists of two separate blocks. The top block has a well-defined back fracture (based on area of movement) with orientation of dip dir. /dip: 297^o /82^o and was bounded by joints dip dir. /dip: 335^o /84^o, 270^o /63^o, 061^o /78^o. Volumes of blocks at B and C were not precisely projected prior to failure due to their relatively small size (in the 100 m^3 range) compared to the blocks at Area A, our inexperience with providing this type of information to CN and the assumption that the potential consequences from Area A would be of more significant concern.

325 **Figure 3**

326 The point cloud difference time series for the three areas are presented in Figure 4. We chose a
327 point representing the greatest amount of deformation for each area in order to plot the time
328 series. The time series of all three areas display a similar evolution of deformation. The greatest
329 observed deformation occurred during the period between 28 November 2013 and 04 June 2014,
330 followed by a period of insignificant ($p > 0.05$) change, between 04 June 2014 and 03 September
331 2014. Area B continued to deform up to the time of data collection in November 2014. We
332 cannot, however, be certain whether significant deformation occurred or not during this interval
333 for areas A and C because the 95% confidence intervals overlap. We did not collect TLS
334 between the November 2014 campaign and the interpreted failure date, 11 December 2014.

335 **Figure 4**

336 We used the 3D block tracking analysis prior to failure of the blocks at A to develop a better
337 understanding of the failure mechanism. We determined the behaviour of blocks B and C from
338 back analysis (Figure 5). For block A, the central blocks deformed 0.09 m over the first 188
339 days, along a plunge of 22° +/- 8° trending 211°. We reported this information to CN on 03
340 September 2014. Our subsequent analysis revealed that the plunge became shallower over time;
341 this can be seen from the decreasing plunge angle and the increasing uncertainty in the plunge
342 angle. The plunge error is greatest for shallow to horizontal plunges because the error is
343 dependent on the ratio between the vertical deformation component and the error in the vertical
344 deformation component. At the time of analysis, we interpreted the movement as a shallow
345 wedge failure along a 22° sliding wedge line.

We characterized the 3D deformation for the top block at Area B by a magnitude of movement between 0.042 and 0.061 m over 347 days, with a shallow plunging angle (seen by the high error in plunge), which was on average negative. The deformation magnitudes of the bottom block ranged between 0.040 – 0.058 m plunging at a shallow angle. The direction of both block deformations trended between 197°-216°. We recorded a topple angle for both blocks reaching 0.6° and 0.9° for the top and bottom block, respectively.

The blocks tracked in Area C registered the smallest deformation of all of the areas, reaching a maximum of 0.019 and 0.026 m for the top and bottom block, respectively, over 347 days. We obtained negative plunges for both blocks with equally high error values. This is due to a small vertical component of deformation relative to the vertical component error; however, in this case the net measured plunge is negative (upwards). Similarly, there is a high error in the trend due to the small horizontal component of deformation relative to the horizontal component error. A maximum topple was recorded of 0.1° for the top block and 0.7° for the bottom block.

Figure 5

Post Failure Analysis and Assessment of Initial Projections

Post failure, we analyzed the three rockfall source zones from the comparison between the OAP-H model collected a few days after the failure, and the pre-failure TLS model. We found that the failure areas corresponded to the previously identified areas of deformation (Figure 6). We calculated a source zone volume at zone A of approximately 4200 m^3, consisting of 3300 m^3 of rock blocks and 900 m^3 of overlying soil. We interpreted the areas of negative model change downslope of Area A to be the result of loss of material due to impact of the rocks sliding down

the slope. We calculated failed volumes for Areas B and C to be approximately 220 m^3 and 210 m^3, respectively.

Most of the rockfall runout was contained by the rockfall protection structure. From analysis of post failure photographs, the debris accumulation from rockfall source Area A appears to cover the debris accumulation below source zone B, indicating that rockfalls from source zone B preceded A. Soil overlying A also overtopped the south (railway west) end of the rockfall protection structure. This prompted the construction of a catchment fence at this location of the structure following the failures.

The projected volume was 14% greater than that measured post failure. The projection of the volume in this case was challenging for two main reasons: (1) the volume of soil affected by the failure of the deforming rocks is difficult to estimate, and (2) there is large uncertainty in where to locate the back scarp plane. The approximate planes and shape of the defining planes used for the analysis can be seen in Figure 6, top right inset. The projected volume estimate in this case was sufficiently accurate to assess the effectiveness of the rockfall protection structure and assess risk mitigation requirements. In this case, CN determined that the structure would provide adequate protection to the rail line for the projected volume of failure.

Figure 6

We analyzed the geological structure exposed in the failure scars to better understand the mechanism of the three failure sites and to assess the accuracy of the kinematics estimated prior to failure, as shown in Figure 7. The post failure planes at A are consistent with those identified prior to failure, and led to wedge-type kinematics, formed from the intersection of joints with dip dir./dip: 238°/46°, 103°/74°,115°/43° with the sliding direction oriented approximately 190°/20°.

389 This is consistent with the trend and plunge obtained using 3D tracking of the blocks,
390 considering the natural variance in joint orientation and the error in the 3D tracking method.

391 Our analysis of the failure scar at Area B revealed that it was controlled by a near vertical back
392 plane with an orientation of 232°/80° (dip/dip dir.). This correlates well with the trend (197° -
393 216°) and shallow plunges observed with the 3D tracking analysis. We interpret this failure as a
394 buckling failure because the upper and lower planar block surfaces were separated by a fracture,
395 there were significant toppling angles, and there was measured upward movement of the top
396 block.

397 The back scarp at Area C measured post failure is 137°/ 82° (dip/dip dir.). The deformation
398 trend, as well as the toppling azimuth, vary between 248°-306°, indicating that this was a
399 toppling failure away from the plane 137°/ 82°.The rotation from 137°/ 82° towards the
400 toppling/deformation direction would have required rotation through 90°, which could explain
401 the upwards measured plunge of deformation.

402 **Figure 7**

403 *Ongoing Monitoring and Projections*

404 Following the failures at Areas A, B and C, our continued monitoring during 2015 revealed
405 additional areas of slope deformation, outlined in Figure 8. Relative to the original baseline scan
406 of 28 November 2013, we observed deformation of areas on either side of the failed block at A,
407 labelled A1 and A2 in Figure 8. We found similar areas adjacent to failed Areas B and C, labeled
408 B1 and C1. We projected volumes of 7, 1000, and 44 m^3 for blocks A1, A2 and B1, respectively.
409 We identified three additional areas of deformation in 2015; Area D, consisting of two separate

deforming blocks D1 and D2, Area E consisting of many separate distinct deforming zones over the area, and Area F consisting of a single zone of deformation. We notified CN of all these deforming areas throughout 2015 (see timeline of events).

We used the deformation time series, the shape of the deforming area, surface roughness and surrounding change to interpret whether measured differences were related to discrete block deformation, accumulation of sediment on the rock surface, or the result of systematic error. We gave notification based on this type of interpretation for all areas that are potentially or could potentially develop into a rock fall source zone, even though the interpretation can change with ongoing monitoring and additional sources of data. Our ongoing monitoring of Areas A1, A2, B1, C1, for example revealed no further development of deformation since the interval where the initial failures occurred. These areas were then no longer interpreted to be blocks showing signs of progressive failure, but rather are interpreted to be a consequence of the failures at A, B and C. The identified blocks were spatially located within the deforming zones of A, B and C prior to failure, the blocks deformed over time along with the blocks that eventually failed, and during the failure interval a large increase in deformation was observed followed by stabilization. Similarly, we re-interpreted the change detected at Areas E and F and found that the change is likely due to accumulation of soil. In the case of zone E, it was being sourced from the soil slope overlying the area. For Area F we interpreted the change as an accumulation of soil due its location within a small gully and characteristic tear drop shape.

We interpreted Area D as a potential rockfall source zone because of its characteristic rock shape and continued increase in measured change. Prior to failure, the deformation time series ends with an increase in the deformation rate during the last scan interval (22 October 2015 – 15 February 2016). We estimated the most probable time of failure of Area D as being during the

spring freeze thaw season after the last scan, because the observed deformation was reaching a critical value as compared to similar failures studied along the main line. This is consistent with Hungr et al's (1999) observation that rockfalls occur at higher frequency during this season in this region. We gave warning to CN with a projected volume of 21 m^3 and 5 m^3 for blocks D1 and D2, respectively. CN performed a risk assessment and determined no action was required due to adequate catchment and the presence of a slide detector fence.

Figure 8

We applied 3D block tracking analysis to the two blocks identified in Area D to better understand the mechanism of failure. We observed a deformation magnitude larger than the limit of detection between 13 September 2014 and 10 November 2014. Following this interval, both blocks continued to deform reaching a maximum of 0.098 m and 0.034 m for blocks D1 and D2, respectively, prior to failure. The error in the plunge is significant for both blocks as a result of a low vertical component of deformation compared to the vertical component error. We calculated a topple angle measuring 1.4° for D1 and 0.5° for D2. We interpreted the failure mechanism for this block to be a topple resulting from detachment from J2 120°/85° (dip dir. /dip).

Figure 9

For each area of deformation, we analyzed surrounding rockfall events. For all but one of the areas we found detectable pre-failure rockfalls surrounding the perimeter of the failure, at potential rockfall source zone D (Figure 10). We observed an increase in rockfalls surrounding both D1 and D2 starting between 04 June 2014 and 03 September 2014. Our monitoring of the total volume at three separate points (1, 2 & 3 in Figure 10) revealed that points 1 and 2 were the

result of discrete rockfall events and that point 3 was the result of an increasing volume from the reference point cloud. This is probably due to increased volume behind the rock block as the back scarp was opening, and may not be the result of loss of physical rock volume.

Figure 10

Failure Area D

The block we identified at Area D failed between TLS scan intervals 22 October 2015 and 15 February 2016 (Figure 11). We estimated the resultant failed volume to be 48.6 m^3, which includes additional failed material surrounding the identified areas of deformation. Due to the larger area involved in the failure, the failed volume was 53% greater than we projected.

Our analysis of the post failure geometry revealed a back scarp at D1 oriented 042°/83° (dip/dip dir) and a back scarp at D2 oriented at 323°/89° (dip/dip dir), corresponding to J4 and J2 respectively. We also observed a sliding plane oriented at 239°/76° (dip/dip dir) linking blocks D1 and D2. The sliding of the block was not apparent prior to failure in this case due to the high error in the plunge angles. The interpreted failure mechanism post failure was slightly different than was projected in this case. Our post failure interpretation of the mechanism was a sliding failure along 239°/76° and a toppling failure in the direction of sliding as a result of the block detachment from 239°/76°and 042°/83°.

Figure 11

Discussion

In this study, we relied on the ability to detect precursors of failure resulting from progressive failure to assess location, magnitude and kinematics of future failures. Compared to previous studies using TLS to detect rock slope deformation (Abellán et al. 2010; Kromer et al. 2015a; Rosser et al. 2007; Royán et al. 2013), precursor rockfalls (Rosser et al. 2005; Stock et al 2012) and tension crack opening (Kromer et al 2015a; Stock et al 2012), we have extended these techniques to estimate the volume and kinematics prior to failure. This is then used in a risk management framework by owners to estimate rockfall risk along an operational rail corridor and to plan appropriate mitigation measures.

Basing our approach on identifying precursors in the damage accumulation phase (Sättele et al. 2015), instead of conducting early warning monitoring (Atzeni et al. 2014; Sättele et al. 2015), permits the monitoring of many sites with the same instrument for a modest field monitoring expense. This is in contrast to early warning monitoring, which requires more frequent or continuous data collection (Kieffer and Valentin 2016), and the identification of the tertiary or acceleration phase of the failure followed by the fitting of models (Crosta and Agliardi 2003; Dick et al. 2015; Fukuzono 1985; Mufundirwa et al. 2010; Voight 1989). Additionally, compared to methods relying solely on the assessment of hazard temporal probability through magnitude frequency (Abott et al. 1998; Hungr et al. 1999; Lato et al. 2011), this approach leads to better decision making through a long term forecast of failure by the identification of incipient failure signs for specific locations with a given magnitude rather than relying on average temporal probabilities from past activity.

We detected a range of precursor activity for different failure mechanisms on this slope. All failure styles resulted in detectable deformation, however precursor rockfalls were only detected in one case around the perimeter of two distinct deforming areas. Similar to observations by Abellán et al. (2010), Rosser et al. (2007) and Royán et al. (2015), we observed that larger rockfalls were preceded by higher deformation. We do, however, note a difference in the nature of precursor activity and the mechanism controlling failure and the fracture planes involved. For example, area D, which was interpreted as a combination of a sliding and toppling mechanism resulted in both detectable precursor rockfalls and a relatively high deformation magnitude for its failed magnitude. Area C, however, was also interpreted as a toppling mechanism and did not result in detectable precursor rockfall nor significant precursor deformation. This suggests that the mechanism of failure and the state of damage accumulation on the failure planes controls the type and magnitude of precursors that can be observed.

The monitoring frequency of this study is sufficient to capture pre-failure deformation and other precursors at this site. This approach only works at slopes that show detectable sings of progressive failure. Due to rock strength, scale of events, joint structure and damage state, some slopes may not exhibit detectable signs prior to failure (Rosser et al. 2007). Our ability to detect precursors is limited by our ability to detect small deformations, by our data collection frequency and by our ability to differentiate block deformation associated with progressive failure from small accumulation of sediment or other processes, or error. TLS data used with high resolution photography can aid in this differentiation by allowing the interpretation of characteristic shape, the calculation of 3D deformation vectors for relatively small rock slope failures and the extraction of deformation time series. Due to our relatively infrequent data collection campaigns, it is likely that we missed detecting a number of precursor rockfalls. The observed accumulation

of rock debris occurring prior to 12 December 2014, for example, is likely due to rockfall precursors to the identified areas, as no other source zone was identified in the comparison between the OAP-H and the TLS models.

The 3D tracking analysis has primarily been used for tracking deformation of large landslide blocks (Oppikoffer et al. 2009), but in this case has been shown to be beneficial in understanding the kinematics of relatively small rockfall failures. The primary limitations are small deformation values in the horizontal or vertical planes or in the toppling angle, which result in a decreased ability to identify meaningful deformation plunges and trends or toppling azimuths, respectively.

The magnitude and kinematics of future events are important parameters for risk assessment and planning risk mitigation options. Our projection of source zone location, volume and kinematics was consistent with an assessment of the post failure scars. In this case, CN determined that the newly built rockfall protection structure would provide sufficient protection against the projected event at A and the existing ditch and warning fence below area D would provide an adequate level of protection. In general, an accurate volume and kinematic estimate can help plan hazard removal options such as scaling and blasting, design stabilization measures such as bolting and design protection methods such as netting and rockfall protection structures. In some cases, the appropriate mitigation option could be the increase in monitoring frequency at a particular site or the installation of a continuous monitoring early warning system.

A more precise estimate of temporal probability can be attained by comparing the state of damage accumulation (i.e. rockmass deformation) to thresholds reached by previous failures of similar nature and by analyzing the influence of environmental factors. Although Rosser et al. (2007) and Royán et al. (2013) have noted a lack of correlation between the tertiary acceleration

phase of failure and environmental triggers at their sites, rockfall activity along this rail line was observed by Peckover and Kerr (1977) as being affected by seasonal climatic effects including freeze-thaw cycles and precipitation. Beginning on 08 December 2014, three days prior to failure of Area A, the region experienced 41 mm of rainfall, which we hypothesize was the primary triggering factor for the failure events. Although we can only constrain the time of failure of blocks at Areas B and C to be between 03 December 2014 and 11 December 2014, we interpreted a failure date during or shortly after this rainfall event as well. Additionally, we observed an apparent link between deformation and weather for Areas A, B, C and D. We believe that environmental triggers such as rainfall and frost jacking, along with slope creep (progressive sliding or brittle fracture propagation) are resulting in damage accumulation and eventual failure of rockfalls at this slope.

Temporal probability of failure can also be better estimated by better understanding the type, magnitude and duration of precursors for different failure modes, magnitudes and in different rock masses. As discussed in Eberhardt et al. (2004) and Rosser et al. (2007), slopes accumulate damage up until a critical threshold, at which point the failure transitions to the tertiary phase leading to collapse. The state of damage of a potential failure can be an indicator of temporal failure probability if critical damage thresholds are known. Potential failures close to the threshold are more likely to progress to the tertiary stage from internal processes such as crack growth and external influences such as environmental triggers. Further study of failure types, magnitude and duration of precursors as a function of failure mode, magnitude and rockmass type can also help us better understand likely failure time.

564

565 ***Conclusions***

566 Monitoring rock slopes at a baseline level (once every 2-4 months) with TLS and supporting
567 remote sensing technologies has great potential to improve rockfall risk management strategies
568 for complex rock slope settings. As shown in this study, it is possible to estimate source zone
569 location, volume and kinematics prior to failure based on the identification of precursor signs of
570 slope failure. The estimation of volumes and mechanisms of future rockfalls is of critical
571 importance for the assessment of consequences and thus risk, and for planning risk mitigation
572 options. Our detection of the failure locations was successful, volume projections were within
573 10-55% of the eventual failure, and the anticipated kinematics and failure mechanism were
574 consistent with that indicated by an assessment of post failure rockfall scar geometries. This
575 strategy can be extended to manage risk from rockfall hazard in mountainous communities or to
576 other sensitive infrastructure.

577 In this study, we move away from defining hazard temporal probability based on magnitude
578 frequency relationships which are based on the long term behavior of the slope. Instead, with the
579 assumption that areas showing precursor signs of failure have a much higher likelihood of failure
580 than that obtained from magnitude frequency relationships, we can specifically locate, assess
581 volume and kinematics of potential rockfalls, before failure occurs. This can be done for many
582 slopes at baseline level.

583 The ability to detect, locate and quantify hazard source zones with accurate volume estimation
584 and kinematics prior to failure has resulted in an improved ability to prioritize mitigation efforts,
585 manage risk, and better understand slope failure mechanisms. This will ultimately improve

586 safety of people and property exposed to many types of slope hazards, particularly rockfall and
587 related landslide types.

588 ***Acknowledgements***

589 We would like to acknowledge support from our funding agencies: CN Rail, Canadian Pacific,
590 Transport Canada and the National Sciences and Engineering Research Council of Canada
591 (NSERC). Special thanks to Matthew Ondercin and Megan van Veen from Queen's University
592 for aid in field data collection; Trevor Evans from CN for organizing helicopter data collection;
593 Chris Bunce from CP for allowing site access; and colleagues from Queen's University for
594 suggestions regarding the written work. We also appreciate the advice and constructive critiques
595 from the two peer reviewers, Dr. Nick Rosser and Dr. Greg Stock.

596

References

Abellán, A., Jaboyedoff, M., Oppikofer, T. and Vilaplana J.M. 2009. Detection of millimetric deformation using a terrestrial laser scanner: experiment and application to a rockfall event. *Natural Hazards and Earth System Science,* 9: 365–372.

Abellán A., Oppikofer T., Jaboyedoff M., Rosser N.J., Lim M. and Lato M.J. 2014. Terrestrial laser scanning of rock slope instabilities. *Earth Surf Process Landforms*, 39(1):80–97.

Abellán A., Vilaplana J.M., Calvet J., García-Sellés D. and Asensio E. 2011. Rockfall monitoring by Terrestrial Laser Scanning – case study of the basaltic rock face at Castellfollit de la Roca (Catalonia, Spain). *Natural Hazards and Earth System Science,* 11(3): 829–841.

Abbott, B., Bruce, I., Keegan, T., Oboni, F. and Savigny, W. 1998. Application of a new methodology for the management of rockfall risk along a railway. *Presented at the 8th Congress, International Assoc. of Engineering Geology, A Global View from the Pacific Rim, Vancouver British Columbia, Balkema, Rotterdam*, vol 2: 1201–1208.

Agisoft. Photoscan. 2014. V1.0. St. Petersburg, Russia.

Atzeni, C., Barla M., Pieraccini M. and Antolini F. 2014. Early Warning Monitoring of Natural and Engineered Slopes with Ground-Based Synthetic-Aperture Radar. *Rock Mechanics and Rock Engineering*, 48(1): 235–246.

Besl, P.J., and McKay, N.D. 1992. Method for registration of 3-D shapes. Proc. SPIE 1611, Sensor Fusion IV: Control Paradigms and Data Structures: 586. doi:10.1117/12.57955.

Corominas, J., van Westen C., Frattini P., Cascini L., Malet J.P., Fotopoulou S., Catani, M., Van Den Eeckhaut, M., Mavrouli, O., Agliardi, F., Pitilakis, K., Winter, M.G., Pastor, M., Ferlisi, S., Tofani,V., Hervás, J., and Smith, J.T. 2014. Recommendations for the quantitative analysis of landslide risk. *Bull Eng Geol Environ*, 73: 209–263. doi:10.1007/s10064-013-0538-8

Crosta, G.B., and Agliardi, F. 2003. Failure forecast for large rock slides by surface displacement measurements. *Canadian Geotechnical Journal,* 40: 176–191.

Dick, G.J., Eberhardt E., Cabrejo-Liévano A.G., Stead D., and Rose N.D. 2015. Development of an early-warning time-of-failure analysis methodology for open-pit mine slopes utilizing ground-based slope stability radar monitoring data. *Canadian Geotechnical Journal*, 52(4): 515–529.

Eberhardt E., Stead D., and Coggan J.S. 2004. Numerical analysis of initiation and progressive failure in natural rock slopes—the 1991 Randa rockslide. *International Journal of Rock Mechanics and Mining Sciences*, 41(1):69–87.

Environment Canada. 2014. Daily Climate Data (Hope). http://climate.weather.gc.ca.

Frayssines, M., and Hantz, D.2006. Failure mechanisms and triggering factors in calcareous cliffs of the Subalpine Ranges (French Alps). *Engineering Geology*, 86(4): 256–270.

Fukuzono, T.1985. A new method for predicting the failure time of a slope. *Proceedings of the 4th International Conference and Field Workshop in Landslides*, Tokyo: 145–150.

Hungr O., Evans S.G., and Hazzard J. 1999. Magnitude and frequency of rock falls and rock slides along the main transportation corridors of southwestern British Columbia. *Canadian Geotechnical Journal*, 36(2): 224–238.

InnovMetric. 2014. PolyWorks V14. Quebec City, Canada.

Jaboyedoff, M., Oppikofer, T., Abellán, A., Derron, M-H., Loye, A., Metzger, R., and Pedrazzini, A.2012. Use of LIDAR in landslide investigations: a review. *Natural Hazards*, 61(1) :5–28.

Kieffer, D.S., Valentin, G. and Unterberger. 2016. Continuous real-time slope monitoring of the Ingelsberg in Bad Hofgastein, Austria. Geomechanics and Tunnelling, 9 (1), 33–44. doi:10.1002/geot.201500047

Kromer, R.A., Hutchinson D.J., Lato M.J., Gauthier D., and Edwards, T.2015a. Identifying rock slope failure precursors using LiDAR for transportation corridor hazard management. *Engineering Geology*, 195: 93–103.

Kromer, R.A., Abellán, A., Hutchinson, D.J., Lato, M., Edwards, T., and Jaboyedoff, M. 2015b. A 4D Filtering and Calibration Technique for Small-Scale Point Cloud Change Detection with a Terrestrial Laser Scanner. *Remote Sensing*, *7*(10): 13029-13052.

Lague, D., Brodu, N. and Leroux, J. 2013. Accurate 3D comparison of complex topography with terrestrial laser scanner: Application to the Rangitikei canyon (NZ). *ISPRS Journal of Photogrammetry and Remote Sensing*, *82*: 10-26.

Lato, M.J., Diederichs, M.S., Hutchinson D.J., and Harrap, R. 2011. Evaluating roadside rockmasses for rockfall hazards using LiDAR data: optimizing data collection and processing protocols. Natural Hazards and Earth System Science, 60: 831–864.

Lato, M.J., Hutchinson, D.J., Gauthier, D., Edwards, T., and Ondercin, M. 2014. Comparison of ALS, TLS and terrestrial photogrammetry for mapping differential slope change in mountainous terrain. *Canadian Geotechnical Journal*, 52(2): 129–140.

Lato, M.J., Gauthier, D., and Hutchinson, D.J. 2015. Rock Slopes Asset Management: Selecting the Optimal Three-Dimensional Remote Sensing Technology. *Transportation Research Record: Journal of the Transportation Research Board*, 2510: 7–14.

MacLaurin, C., Mahoney, J., Harggart, J., Goodin, J., and Mustard, P. 2011. The Jackass Mountain Group of south-central British Columbia: depositional setting and evolution of an early Cretaceous deltaic complex. *Canadian Journal of Earth Sciences,* 48: 930–951.

Mufundirwa, A., Fujii, Y., and Kodama, J. 2010. A new practical method for prediction of geomechanical failure-time. *International Journal of Rock Mechanics and Mining Sciences*, 47(7):1079.

Oppikofer, T., Jaboyedoff, M., Blikra, L., Derron, M.H., and Metzger, R. 2009. Characterization and monitoring of the Åknes rockslide using terrestrial laser scanning. *Natural Hazards and Earth System Science*, 9: 1003–1019.

Oppikofer, T., Jaboyedoff, M., and Keusen, H-R. 2008. Collapse at the eastern Eiger flank in the Swiss Alps. *Nature Geoscience*, 1: 531–535.

Peckover, F.L., and Kerr, J.W.G. 1977. Treatment and maintenance of rock slopes on transportation routes. *Canadian Geotechnical Journal*, 14: 487–507.

Rabatel, A., Deline, P., Jaillet, S., and Ravanel, L. 2008. Rock falls in high-alpine rock walls quantified by terrestrial lidar measurements: A case study in the Mont Blanc area. *Geophysical Research Letters*, 35(10).

Rosser, N., Lim, M., Petley, D., Dunning, S., and Allison, R. 2007. Patterns of precursory rockfall prior to slope failure. *Journal of Geophysical Research*, 112.

Royán, M.J., Abellán, A., Jaboyedoff, M., Vilaplana, J.M., and Calvet, J. 2013. Spatio-temporal analysis of rockfall pre-failure deformation using Terrestrial LiDAR. *Landslides,* 11: 697–709.

Royán, M. J., Abellán, A., and Vilaplana, J. M. 2015. Progressive failure leading to the 3 December 2013 rockfall at Puigcercós scarp (Catalonia, Spain). *Landslides*, 12(3): 585–595.

Sättele, M., Krautblatter, M., Bründl, M., and Straub D. 2015. Forecasting rock slope failure: how reliable and effective are warning systems? Landslides: 1–14 doi: 10.1007/s10346-015-0605-2

Stock, G.M., Bawden, G.W., Green, J.K., Hanson, E., Downing, G., Collins, B.D., Bond, S., and Leslar, M. 2011. High-resolution three-dimensional imaging and analysis of rock falls in Yosemite Valley, California. *Geosphere*, 7(2):573–581.

Stock, G.M., Martel, S.J., Collins, B.D., and Harp, E.L. 2012. Progressive failure of sheeted rock slopes: the 2009-2010 Rhombus Wall rock falls in Yosemite Valley, California, USA. E*arth Surface Processes and Landforms,* 37: 546–561.

Sturzenegger, M., Keegan, T., Wen, A., Willms, D. Stead, D., and Edwards T. 2014. LiDAR and Discrete Fracture Network Modeling for Rockslide Characterization and Analysis. *In Engineering Geology for Society and Territory* - Volume 6 , Lollino G, Giordan D, Thuro K,

Sturzenegger, M., and Stead, D. 2009. Close-range terrestrial digital photogrammetry and terrestrial laser scanning for discontinuity characterization on rock cuts. *Engineering Geology,* 106: 163–182.

Teledyne Optech. 2014. Ilris Terrestrial Laser Scanner [Internet]. Available from: http://www.teledyneoptech.com/wp-content/uploads/ILRIS-Spec-Sheet-140730-WEB.pdf

Teza, G., Galgaro, A., Zaltron, N., and Genevois, R. 2007. Terrestrial laser scanner to detect landslide displacement fields: a new approach. *International Journal of Remote Sensing,* 28: 3425–3446.

Voight, B.1989. A Relation to Describe Rate-Dependent Material Failure. *Science*, 243(4888):200–203

Figure Captions

Figure 1: Top left: Site location in the Fraser Valley in British Columbia. Bottom left: Oblique helicopter photogrammetry (OAP-H) model of the slope from 14 December 2014, including the new rock protection structure. Top right: location of the monitored area on an ALS DEM, showing position relative to the Canadian National Rail line and the TransCanada Highway. Bottom right is the rockmass structure of the study site as analyzed by Sturzenegger et al. (2014).

Figure 2: Timeline data collection, events observed and action taken. Top Photo: Areas where slope deformation was identified. The events that occurred during the top part of the timeline (day 0-381) are described in the "Initial Projection and Failure Warning" section and the events from day 381 onwards, shown in the bottom half of the timeline, are described in the "Ongoing Monitoring and Projections" section.

Figure 3: Identification and analysis of slope deformation in three distinct Areas A, B and C. Top: Filtered positive point cloud differences along slope dependent normal vector from reference scan 28 November 2013 to 04 June 2014. Bottom: Cumulative time series of identified areas of positive change prior to failure. Other observed slope changes are due to construction of the rockfall protection structure and accumulation of rock debris and soil (annotated in top image).

Figure 4: Time series of positive point cloud differences along slope dependent normal vector at the point of maximum difference in Areas A, B and C between 28 November 2013 and 10

November 2014 (0-347 days). Interpreted failure date is indicated by a yellow star. Bottom graph: Cumulative precipitation for the same time period.

Figure 5: 3D block tracking analysis of deforming blocks at Areas A, B and C. Left images show points used for 3D tracking analysis in colour. Right tables show the translation component of the center point of the tracked block as magnitude, trend and plunge of translation vector, and the rotation component as the angle between a vertical vector and the topple vector, azimuth of topple vector and rotation around topple vector (tilt).

Figure 6: Analysis of slope post failure and assessment of initial projections. Top left: Change detection map between reference TLS scan (28 November 2013) and OAP-H data (14 December 2014). Bottom left: Photograph showing rockfall source zones and accumulation of rock and soil debris. Right column: TLS model of source zones prior to failure, overlain on after failure photogrammetry model and failed volumes for Areas A, B, and C. Areas of failure correspond to projected source zones outlined in Figure 3.

Figure 7: Equal Area stereonets of structure at post failure source zones for Areas A, B and C.

Figure 8: Identification and analysis of slope deformation after initial failures. Top: Filtered positive point cloud differences along the slope based on a comparison between the reference scan from 28 November 2013 with 22 October 2015. Bottom: Time series of cumulative positive point cloud differences along a slope dependent normal vector at the point of maximum difference in each respective area.

Figure 9: 3D block tracking analysis of deforming blocks at Area D. Left image shows points used for 3D tracking analysis in colour. Right tables show the translation component of the center point of the tracked block as magnitude, trend and plunge of translation vector, and the rotation component as the angle between a vertical vector and the topple vector, azimuth of topple vector and rotation around topple vector (tilt).

Figure 10: Analysis of precursor rockfalls around the perimeter of deforming blocks at Area D. Rockfall surface areas are represented by coloured points associated with a comparison period. Volumes of the 3 rockfall areas are plotted as well as deformation at point D1.

Figure 11: Post failure of block at Area D. A, TLS image showing failure at D between 22 October 2015 and 15 February 2016; B, before failure photograph taken on 11 June 2015; and C, after failure photograph taken on 15 February 2016.

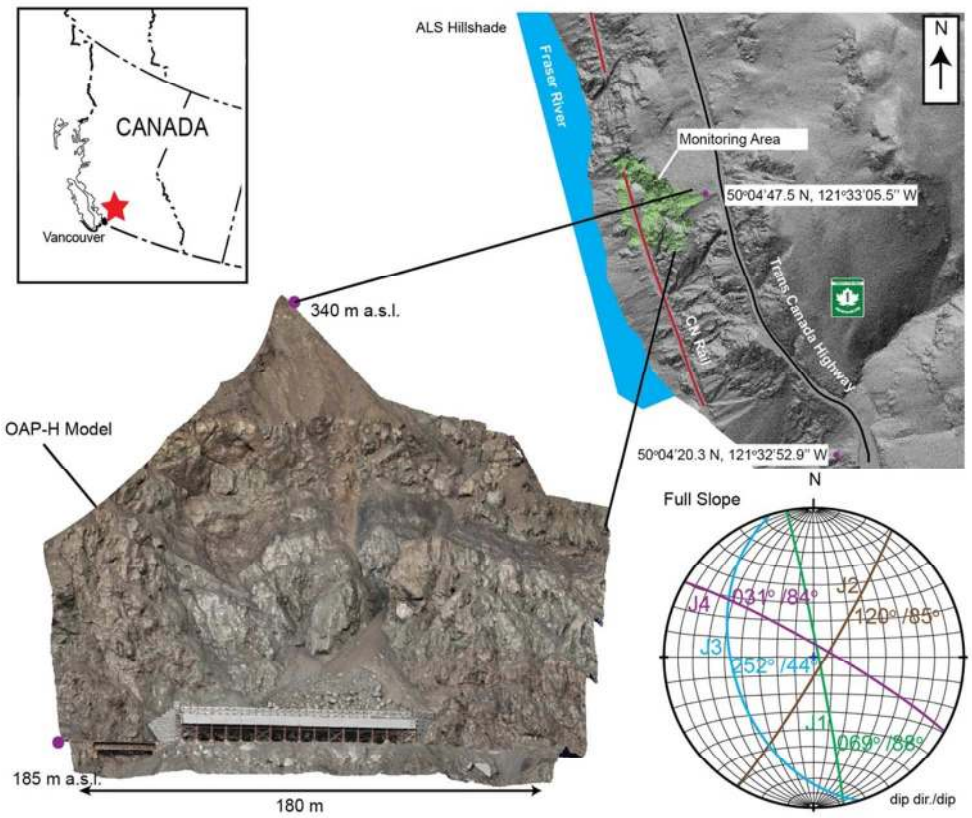

Figure 1: Top left: Site location in the Fraser Valley in British Columbia. Bottom left: Oblique helicopter photogrammetry (OAP-H) model of the slope from 14 December 2014, including the new rock protection structure. Top right: location of the monitored area on an ALS DEM, showing position relative to the Canadian National Rail line and the TransCanada Highway. Bottom right is the rockmass structure of the study site as analyzed by Sturzenegger et al. (2014).

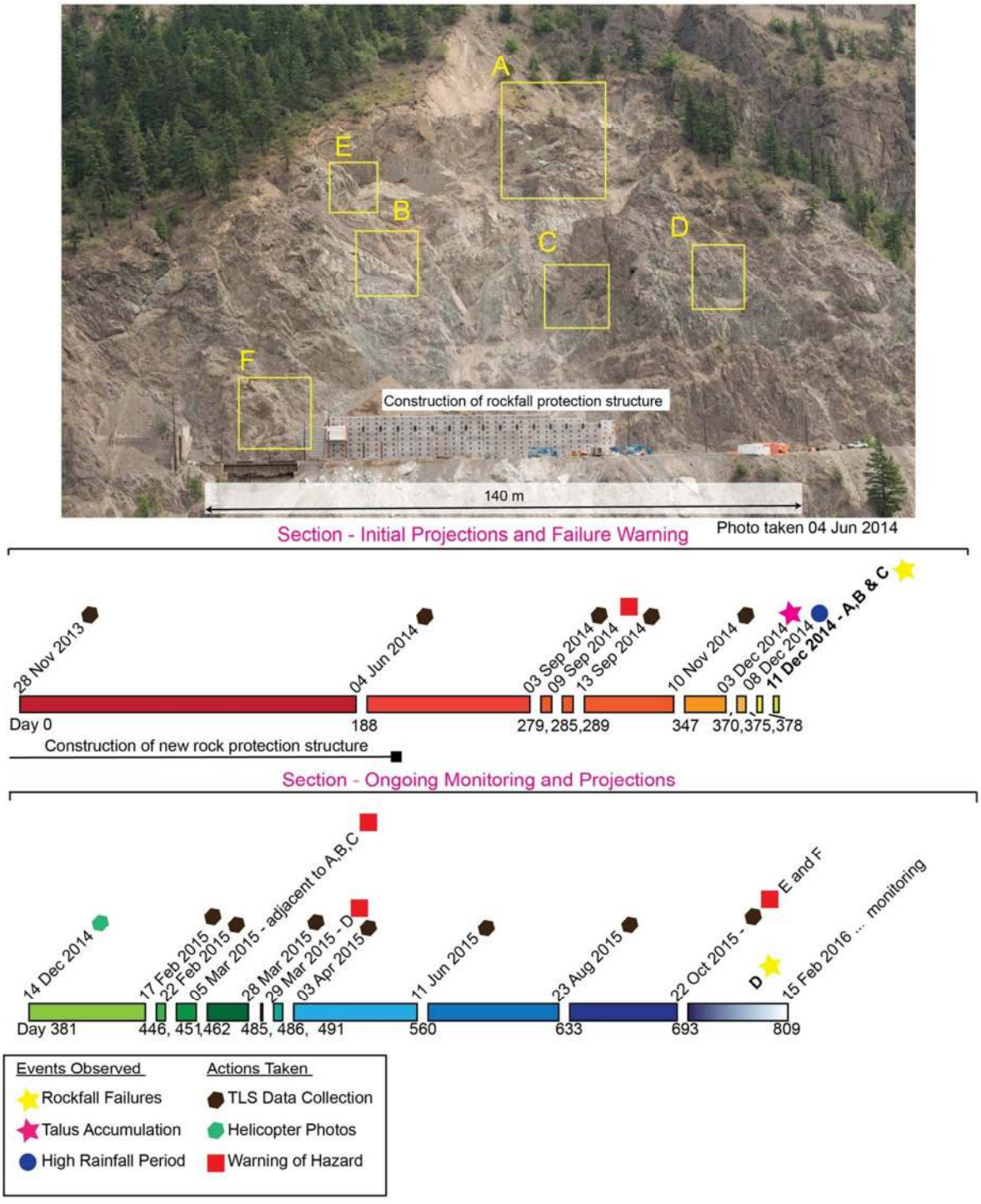

Figure 2: Timeline data collection, events observed and action taken. Top Photo: Areas where slope deformation was identified. The events that occurred during the top part of the timeline (day 0-381) are described in the "Initial Projection and Failure Warning" section and the events

from day 381 onwards, shown in the bottom half of the timeline, are described in the "Ongoing Monitoring and Projections" section.

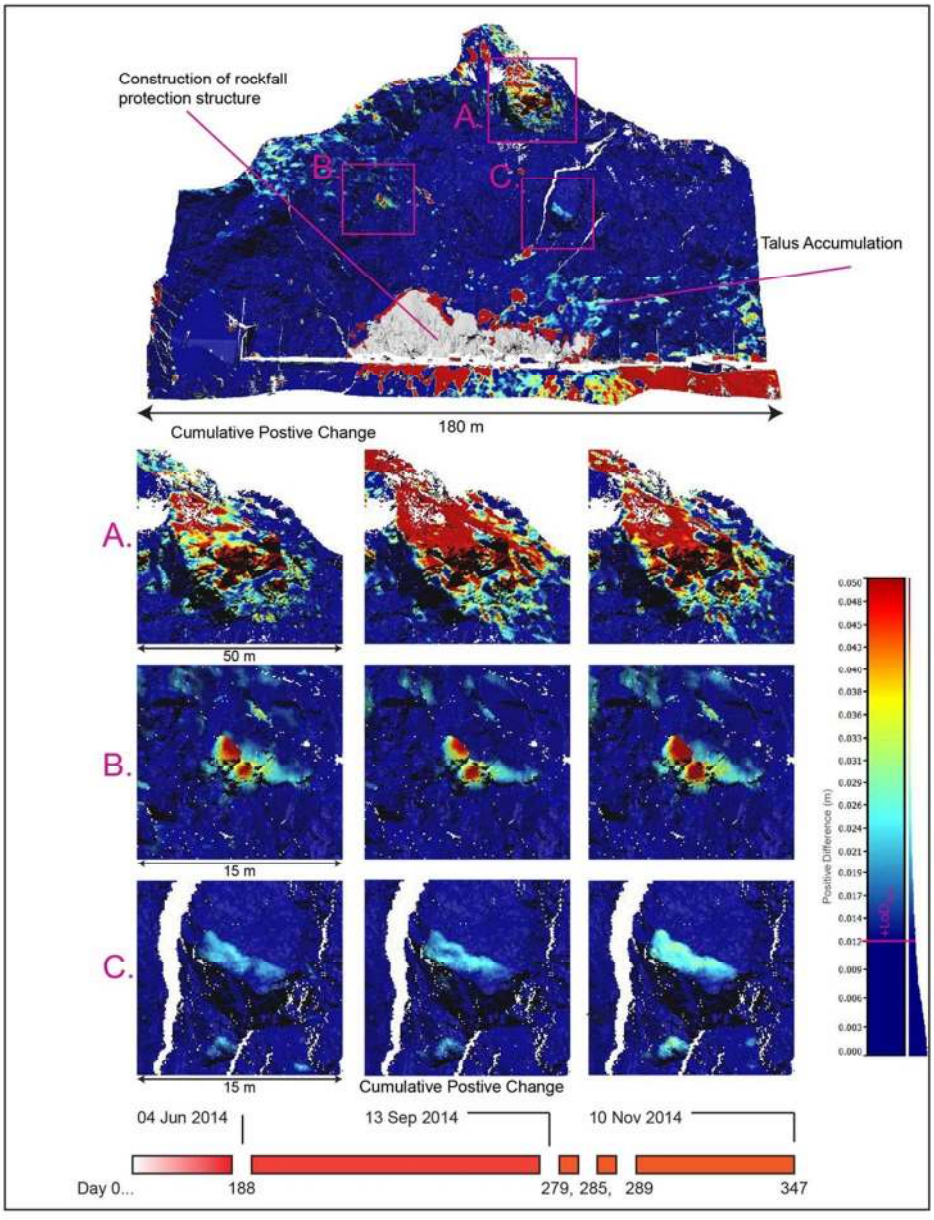

Figure 3: Identification and analysis of slope deformation in three distinct Areas A, B and C. Top: Filtered positive point cloud differences along slope dependent normal vector from reference scan 28 November 2013 to 04 June 2014. Bottom: Cumulative time series of identified areas of positive change prior to failure. Other observed slope changes are due to construction of the rockfall protection structure and accumulation of rock debris and soil (annotated in top image).

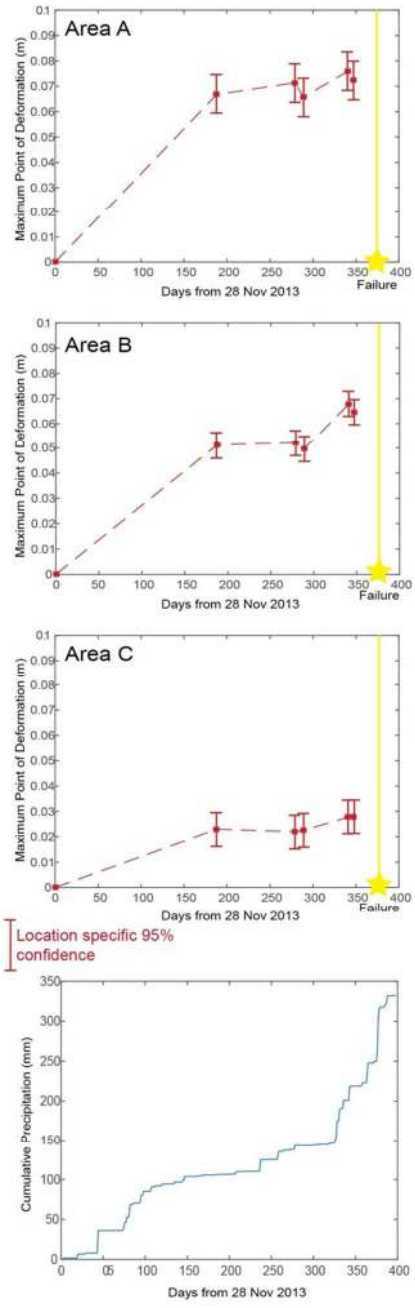

Figure 4: Time series of positive point cloud differences along slope dependent normal vector at the point of maximum difference in Areas A, B and C between 28 November 2013 and 10 November 2014 (0-347 days). Interpreted failure date is indicated by a yellow star. Bottom graph: Cumulative precipitation for the same time period.

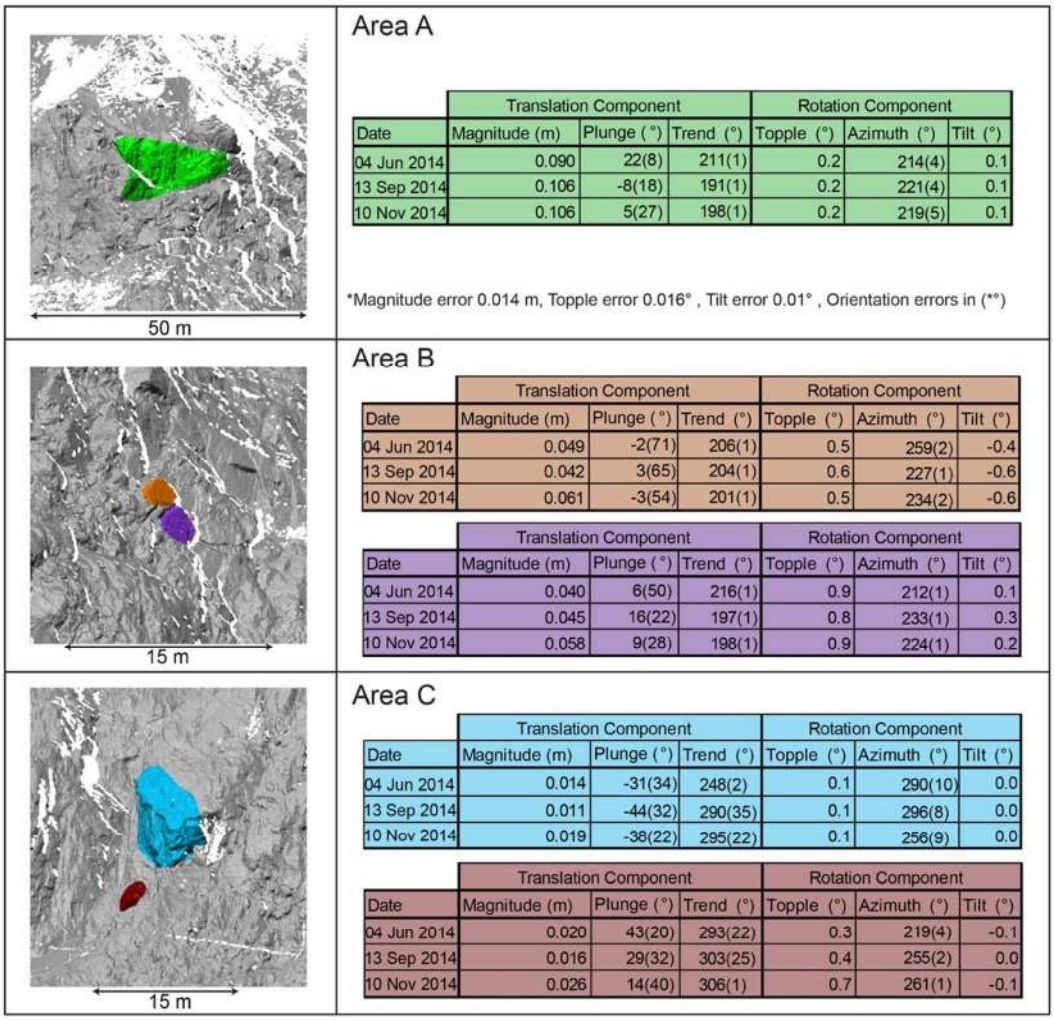

Area A

Date	Translation Component			Rotation Component		
	Magnitude (m)	Plunge (°)	Trend (°)	Topple (°)	Azimuth (°)	Tilt (°)
04 Jun 2014	0.090	22(8)	211(1)	0.2	214(4)	0.1
13 Sep 2014	0.106	-8(18)	191(1)	0.2	221(4)	0.1
10 Nov 2014	0.106	5(27)	198(1)	0.2	219(5)	0.1

*Magnitude error 0.014 m, Topple error 0.016° , Tilt error 0.01° , Orientation errors in (**)

Area B

Date	Translation Component			Rotation Component		
	Magnitude (m)	Plunge (°)	Trend (°)	Topple (°)	Azimuth (°)	Tilt (°)
04 Jun 2014	0.049	-2(71)	206(1)	0.5	259(2)	-0.4
13 Sep 2014	0.042	3(65)	204(1)	0.6	227(1)	-0.6
10 Nov 2014	0.061	-3(54)	201(1)	0.5	234(2)	-0.6

Date	Translation Component			Rotation Component		
	Magnitude (m)	Plunge (°)	Trend (°)	Topple (°)	Azimuth (°)	Tilt (°)
04 Jun 2014	0.040	6(50)	216(1)	0.9	212(1)	0.1
13 Sep 2014	0.045	16(22)	197(1)	0.8	233(1)	0.3
10 Nov 2014	0.058	9(28)	198(1)	0.9	224(1)	0.2

Area C

Date	Translation Component			Rotation Component		
	Magnitude (m)	Plunge (°)	Trend (°)	Topple (°)	Azimuth (°)	Tilt (°)
04 Jun 2014	0.014	-31(34)	248(2)	0.1	290(10)	0.0
13 Sep 2014	0.011	-44(32)	290(35)	0.1	296(8)	0.0
10 Nov 2014	0.019	-38(22)	295(22)	0.1	256(9)	0.0

Date	Translation Component			Rotation Component		
	Magnitude (m)	Plunge (°)	Trend (°)	Topple (°)	Azimuth (°)	Tilt (°)
04 Jun 2014	0.020	43(20)	293(22)	0.3	219(4)	-0.1
13 Sep 2014	0.016	29(32)	303(25)	0.4	255(2)	0.0
10 Nov 2014	0.026	14(40)	306(1)	0.7	261(1)	-0.1

Figure 5: 3D block tracking analysis of deforming blocks at Areas A, B and C. Left images show points used for 3D tracking analysis in colour. Right tables show the translation component of the center point of the tracked block as magnitude, trend and plunge of translation vector, and the rotation component as the angle between a vertical vector and the topple vector, azimuth of topple vector and rotation around topple vector (tilt).

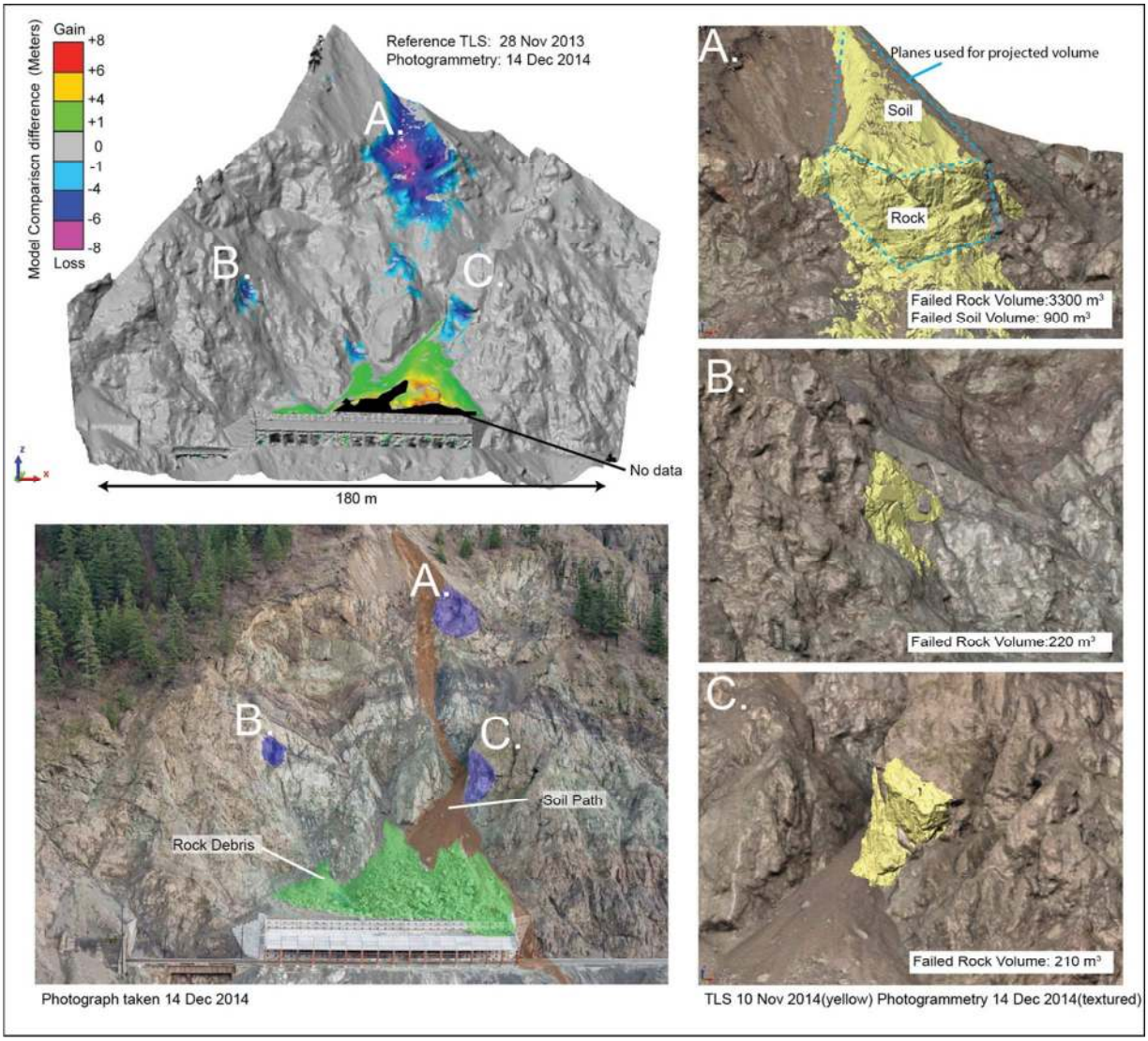

Figure 6: Analysis of slope post failure and assessment of initial projections. Top left: Change detection map between reference TLS scan (28 November 2013) and OAP-H data (14 December 2014). Bottom left: Photograph showing rockfall source zones and accumulation of rock and soil debris. Right column: TLS model of source zones prior to failure, overlain on after failure photogrammetry model and failed volumes for Areas A, B, and C. Areas of failure correspond to projected source zones outlined in Figure 3.

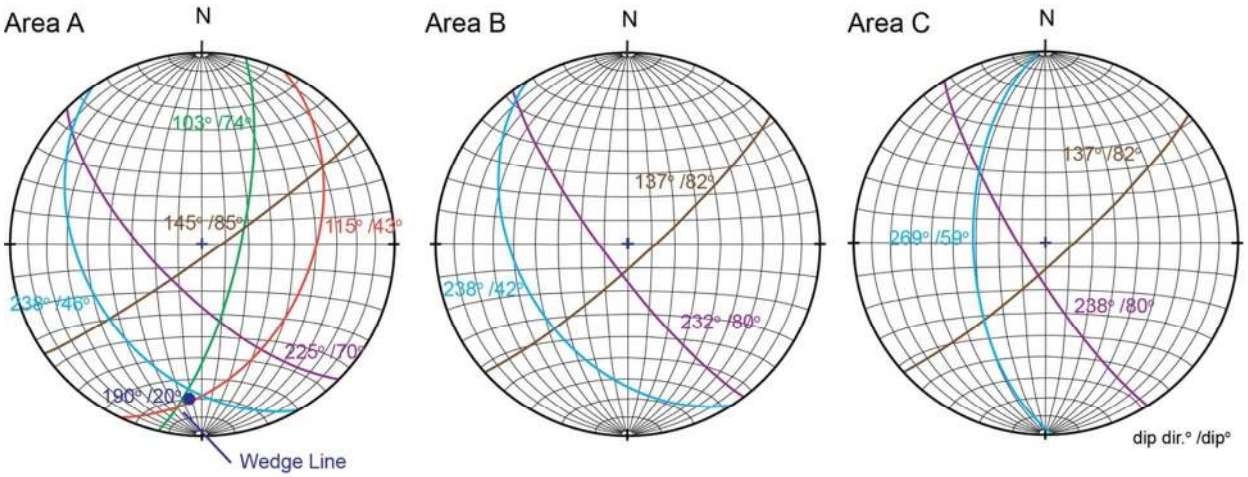

Figure 7: Equal Area stereonets of structure at post failure source zones for Areas A, B and C.

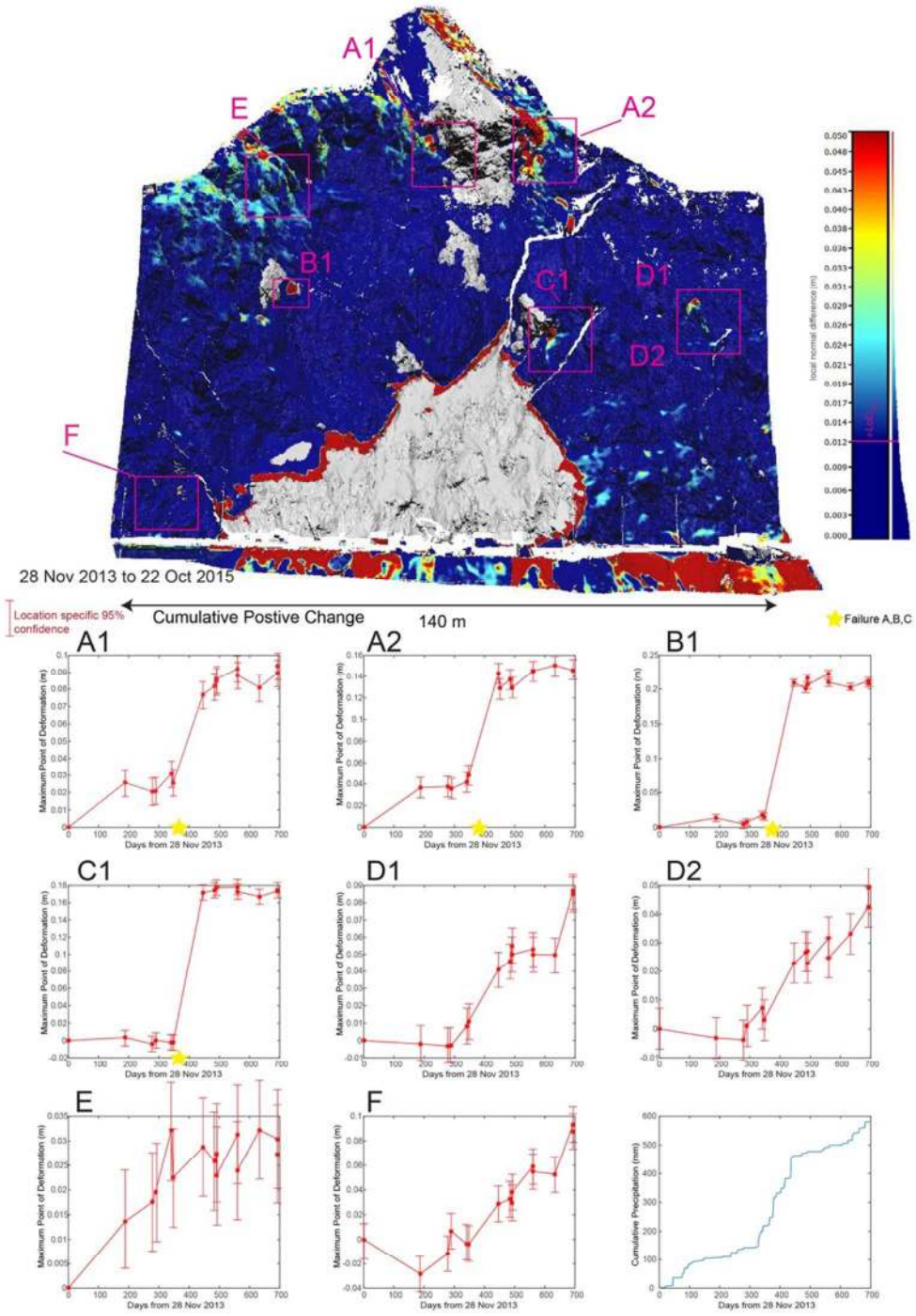

Figure 8: Identification and analysis of slope deformation after initial failures. Top: Filtered positive point cloud differences along the slope based on a comparison between the reference scan from 28 November 2013 with 22 October 2015. Bottom: Time series of cumulative positive point cloud differences along a slope dependent normal vector at the point of maximum difference in each respective area.

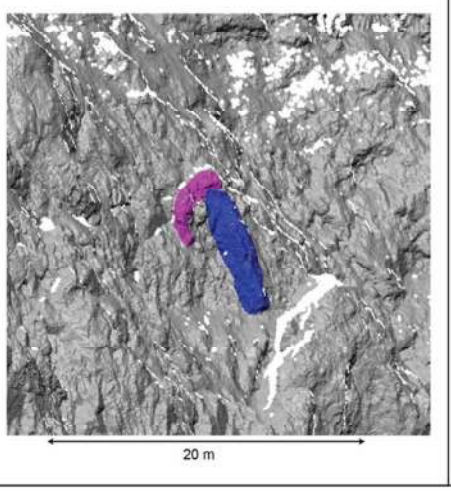

Area D

	Translation Component			Rotation Component		
Date	Magnitude (m)	Plunge (°)	Trend (°)	Topple (°)	Azimuth (°)	Tilt (°)
04 Jun 2014	-0.012	29(42)	116(2)	0.1	172(7)	0.2
13 Sep 2014	0.003	11(93)	270(58)	0.2	251(6)	0.4
10 Nov 2014	0.014	-27(39)	286(24)	0.3	224(3)	0.3
17 Feb 2015	0.047	-9(33)	283(7)	0.7	265(1)	0.4
28 Mar 2015	0.057	-6(42)	291(6)	0.8	264(1)	0.7
03 Apr 2015	0.057	-14(20)	293(6)	0.8	269(1)	0.5
11 Jun 2015	0.057	-9(30)	289(6)	0.8	276(1)	0.5
22 Oct 2015	0.098	4(37)	288(3)	1.4	275(1)	0.8

	Translation Component			Rotation Component		
Date	Magnitude (m)	Plunge (°)	Trend (°)	Topple (°)	Azimuth (°)	Tilt (°)
04 Jun 2014	0.013	-35(34)	145(47)	0.0	266(90)	-0.1
13 Sep 2014	0.013	-23(44)	59(24)	0.0	303(24)	-0.2
10 Nov 2014	0.016	-38(27)	35(30)	0.1	198(7)	-0.1
17 Feb 2015	0.026	-53(14)	15(38)	0.2	269(5)	-0.3
28 Mar 2015	0.026	-22(27)	356(68)	0.2	252(4)	-0.3
03 Apr 2015	0.036	-28(17)	5(34)	0.3	278(3)	-0.3
11 Jun 2015	0.035	-15(29)	2(38)	0.3	241(3)	-0.4
22 Oct 2015	0.034	-9(42)	356(58)	0.5	265(2)	-0.4

*Magnitude error 0.014 m, Topple error 0.016° , Tilt error 0.01° , Orientation errors in (°°)

Figure 9: 3D block tracking analysis of deforming blocks at Area D. Left image shows points used for 3D tracking analysis in colour. Right tables show the translation component of the center point of the tracked block as magnitude, trend and plunge of translation vector, and the rotation component as the angle between a vertical vector and the topple vector, azimuth of topple vector and rotation around topple vector (tilt).

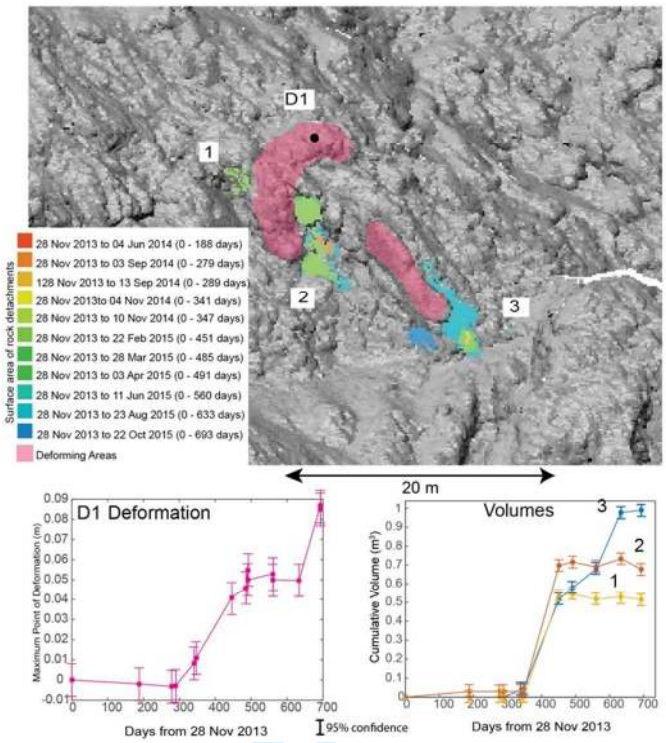

Figure 10: Analysis of precursor rockfalls around the perimeter of deforming blocks at Area D. Rockfall surface areas are represented by coloured points associated with a comparison period. Volumes of the 3 rockfall areas are plotted as well as deformation at point D1.

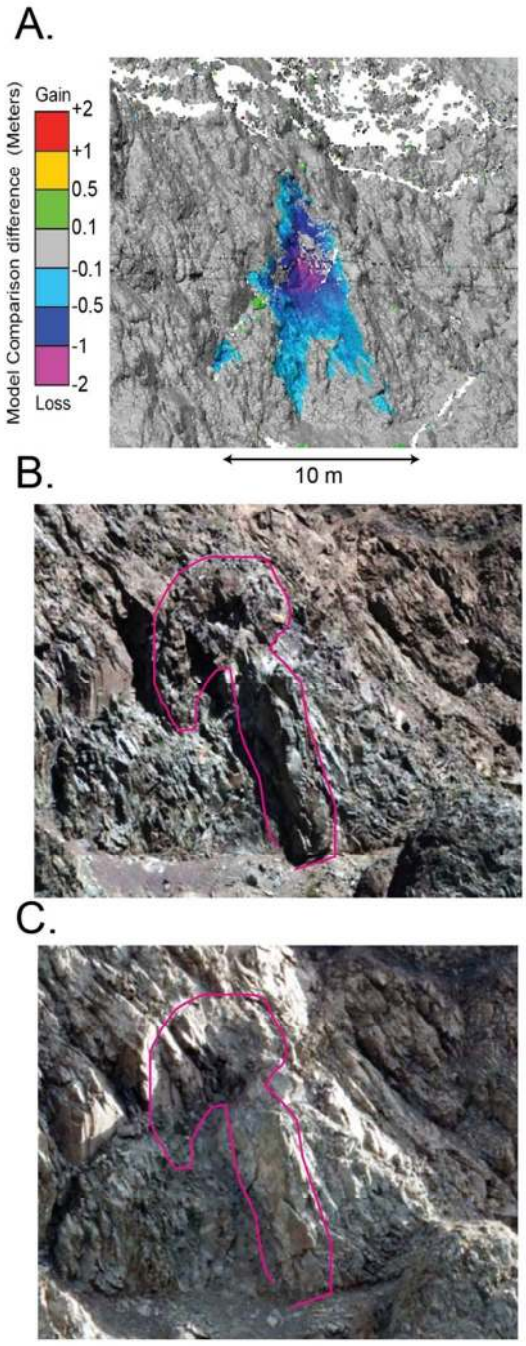

Figure 11: Post failure of block at Area D. A, TLS image showing failure at D between 22 October 2015 and 15 February 2016; B, before failure photograph taken on 11 June 2015; and C, after failure photograph taken on 15 February 2016.